Multipolar Analysis in Symmetrical Meta-Atoms Sustaining Fano Resonances

optics

MDPI

Communication

Multipolar Analysis in Symmetrical Meta-Atoms Sustaining Fano Resonances

Vittorio Bonino [1] and Angelo Angelini [2,*]

[1] Dipartimento di Scienza Applicata e Tecnologia (DISAT), Politecnico di Torino, C.so Duca degli Abruzzi 24, 10129 Turin, Italy; vittorio.bonino@polito.it
[2] Advanced Materials and Life Sciences Division, Istituto Nazionale di Ricerca Metrologica, Strada delle Cacce 91, 10135 Turin, Italy
* Correspondence: a.angelini@inrim.it

Abstract: We present an optical metasurface with symmetrical individual elements sustaining Fano resonances with high Q-factors. This study combines plane-wave illumination and modal analysis to investigate the resonant behavior that results in a suppression of the forward scattering, and we investigate the role of the lattice constant on the excited multipoles and on the spectral position and Q-factor of the Fano resonances, revealing the nonlocal nature of the resonances. The results show that the intrinsic losses play a crucial role in modulating the resonance amplitude in specific conditions and that the optical behavior of the device is extremely sensitive to the pitch of the metasurface. The findings highlight the importance of near-neighbor interactions to achieve high Q resonances and offer an important tool for the design of spectrally tunable metasurfaces using simple geometries.

Keywords: all-dielectric metasurfaces; Mie resonances; Kerker condition

Citation: Bonino, V.; Angelini, A. Multipolar Analysis in Symmetrical Meta-Atoms Sustaining Fano Resonances. *Optics* **2024**, *5*, 238–247. https://doi.org/10.3390/opt5020017

Received: 9 February 2024
Revised: 8 March 2024
Accepted: 1 April 2024
Published: 15 April 2024

1. Introduction

The ability to engineer light scattering with high efficiency and low losses by patterning dielectric thin films [1] has enabled a number of technological applications ranging from substituting bulk optical devices with flat optical elements to shape the wavefront of light both in the linear [2] and nonlinear [3–5] regimes to lasing [6], structural colors [7], sensing [8–10], optical modulation [11,12], and quantum optics [13].

The rapidly growing success of dielectric metasurfaces [14–16] and the rising interest of private companies toward their potential for the consumer market [17] have fostered an intense effort to design individual subwavelength elements to engineer their scattering properties and tailor their interaction with light [18,19]. Several concepts of metadevices have indeed been proposed in the literature, including actively tunable devices working in different spectral ranges [20–22]. Artificial intelligence has also been explored as a tool for designing complicated subwavelength scatterers that exhibit optimized far-field performances [23–25]. However, increasing the complexity of the design results in increased costs and efforts for fabrication, which becomes more and more challenging when approaching the visible regime [26,27]. One of the key factors underlying the success of photonic metasurfaces is indeed the possibility to exploit fabrication techniques derived from micro- and nanoelectronics, where the need for cost-effective and large-scale production is crucial and has pushed the research to move from standard lithographic techniques such as electron beam lithography toward deep UV lithography, nanoimprinting, and self-assembling techniques [28].

Optical devices based on a dielectric metasurface may rely on different working principles, and a number of comprehensive reviews can now be found in the literature that describe the different types of metasurfaces [29–32]. In this work, we discuss the case of a metasurface that sustains Mie resonances in the visible range. According to the Kerker conditions [33], by exciting Mie resonances and eventually combining them, a complete

suppression of the forward- or backward-scattered field [34] can be achieved, as well as bound states in a continuum [35,36]. Moreover, the combination of localized multipolar resonances with nonlocal distributed resonances supported by arrays of an individual nanoscatterer enables the excitation of high-Q Fano resonances that can greatly boost the field enhancement over large volumes [37].

In this framework, our work aims at two distinct goals: firstly, we provide an insight on the resonant mechanism of a lattice of dielectric resonators, highlighting the nonlocal nature of the multipolar resonances by analyzing their dependence on the lattice constant. Secondly, we show that a simple and symmetric design can exhibit high-Q Fano resonances and that such Fano resonances are mechanically tunable, for example, by changing the periodicity of the metasurface. Such tunability can also be exploited in a simple strain-sensing scheme with optical readout, and at the end of the paper, we provide the sensitivity and the figure of merit for the proposed strain sensor. In addition to sensing, for the discussed metasurface, we foresee particularly interesting applications in transmitted-light-intensity modulation and spectrally tunable transmission filters. The great advantage of having such a design of an individual nanoscatterer lies in the possibility to use self-assembling approaches such as nanosphere lithography [38,39] or block copolymer technology [40–43]. Such techniques are scalable and can be used to fabricate metasurfaces over large areas with high throughput, thus reducing the effective cost of metasurface-based optical devices for industrial applications.

2. Materials and Methods

The optical properties of the metasurface were investigated using COMSOL Multiphysics 6.0, with the RF module in the Frequency domain. The simulated structure is sketched in Figure 1a: a square lattice of cylindrical nanopillars of diameter $d = 270$ nm, height $h = 540$ nm, and complex refractive index taken from [44] and plotted in Figure 1b. We would like to highlight that such values are also achievable with different materials such as diamond, silicon nitride, or high index metallic oxides. The nanopillars lying on a lossless optical glass substrate ($n = 1.51$) [45] and surrounded by air ($n = 1$) were illuminated by a plane wave normally impinging on the surface and polarized along x. The complex refractive index of the nanopillars accounted for losses that can be intrinsic or due to random scattering introduced by roughness in real-world applications, while other types of defects that can lead to broadening of the resonances were not taken into account. The free-space wavelength varied from 640 to 700 nm, and for each wavelength, we computed the reflectance, transmittance, absorbance, electric field distribution, and contribution to the scattering cross section of the different multipoles. The Q-factor was calculated by performing modal analysis in COMSOL. The lattice was modeled by applying periodic boundary conditions (Floquet periodicity) along x and y. The simulated domain was decomposed in a mesh with maximum and minimum element sizes of $1/5$ and $1/50$ of the effective wavelength, respectively. The lattice constant P was varied to investigate the role of the periodicity on the optical response of the metasurface, while the other geometrical parameter was kept fixed.

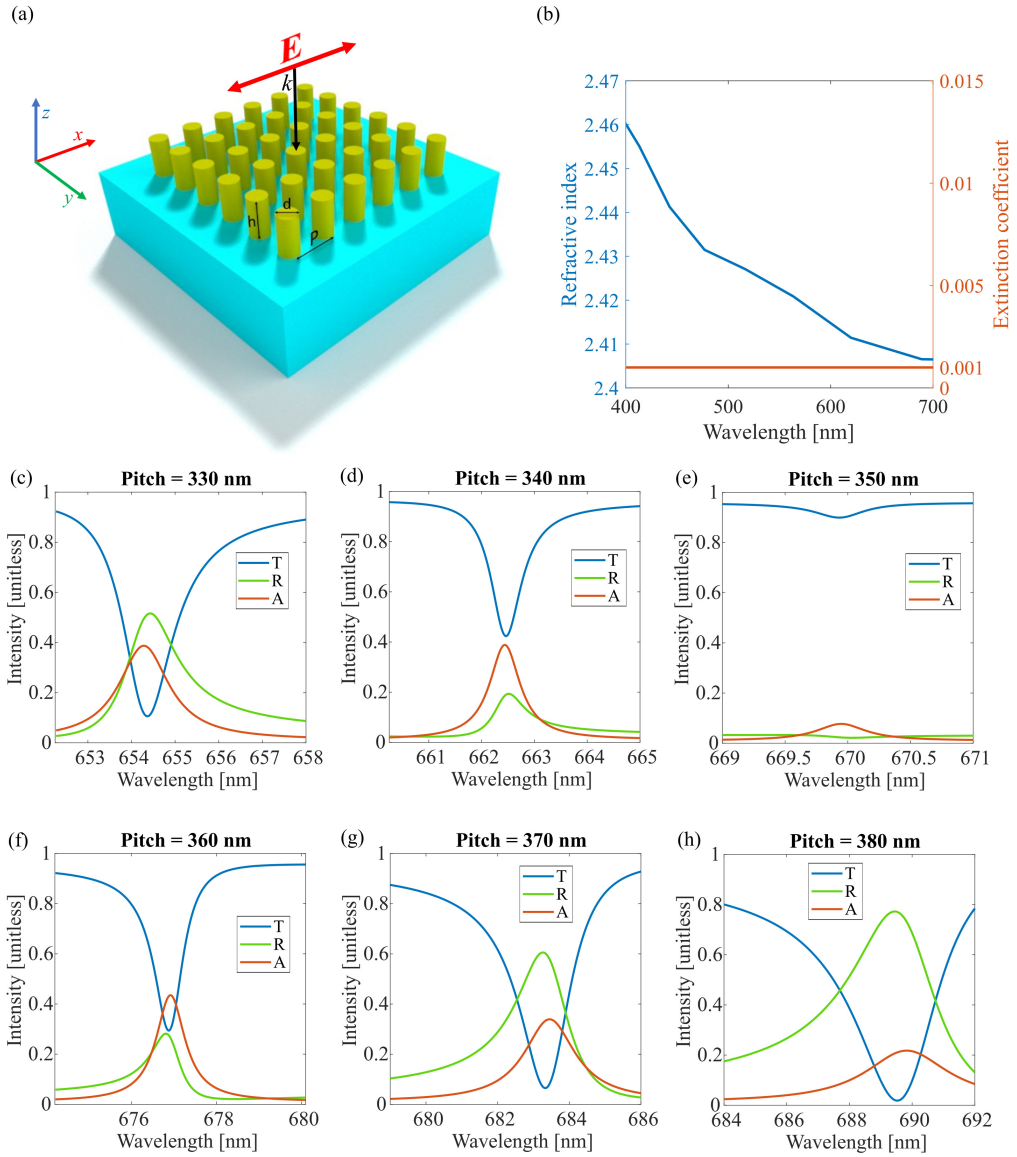

Figure 1. (**a**) Three-dimensional schematic of the simulated metasurface. (**b**) Real (blue) and imaginary (red) part of the refractive index used for the nanopillars. (**c**–**h**) Graphs showing transmission (blue line), reflection (green line), and absorption (red line) as functions of wavelength for the metasurface, with pitches ranging from 330 nm to 380 nm.

3. Results

At first, we calculated the transmittance, reflectance, and absorption in the spectral range about the resonance at different values of the lattice constant P (Figure 1c–h).

The plots unveil the existence of Fano resonances sustained by the cylindrical structures resulting in attenuated transmittance at the resonant wavelength. Such resonances were reported in a recent paper in which the ideal case of lossless nanopillars was considered [46]. By including in the model a complex refractive index, we show that absorption within the nanopillar is also enhanced, suggesting that light–matter interaction is boosted within the nanopillars. In detail, as the pitch P approaches the value of 350 nm, the resonance undergoes a redshift and absorption increases up to a value of about 40%, while the dip in transmittance is progressively attenuated. At $P = 350$ nm, the resonance almost vanishes and the absorption falls below 10%. It is worth noticing that such strong variation of the resonance depth is inherently related to the intrinsic losses included in the model,

for such behavior was not observed in previous studies where intrinsic losses were neglected [46,47]. By further increasing the pitch, the absorption and the transmittance dip increase again, reaching almost zero transmittance at $P = 380$ nm. The resonance observed can be well described by the Fano formula:

$$T(f) = \frac{(\Omega + q)^2(1 + q)^2}{(\Omega^2 + 1)} \quad (1)$$

where $\Omega = 2 \times \frac{f - f_0}{\gamma}$ contains the resonance frequency (f_0) and the resonance width (γ), and q is the Fano parameter. Notably, the typical asymmetry associated with the Fano resonances and described by the Fano parameter [48,49] changes sign when the pitch crosses the value of 350 nm.

To further investigate the resonant behavior of the metasurface, we expressed the scattered field as a superposition of the field generated by multipolar sources according to the Mie theory [50]:

$$\mathcal{C}_{sca}^{total} = \mathcal{C}_{sca}^{ED} + \mathcal{C}_{sca}^{MD} + \mathcal{C}_{sca}^{EQ} + \mathcal{C}_{sca}^{ME} + \ldots \quad (2)$$

where the total scattering cross section can be expressed as the sum of contributions of electric and magnetic dipoles (ED, MD) quadrupoles (EQ, MQ), and higher-order multipoles. The individual contribution of each multipole is calculated according to the following expressions, derived in recent papers [51,52]:

$$a_E(l,m) = \frac{(-i)^{l-1}k^2\eta O_{lm}}{E_0[\pi(2l+1)]^{1/2}} \int e^{-im\phi}[\psi_l(kr) + \psi_l''(kr)]P_l^m(\cos\theta)\hat{r} \times \mathbf{J}_{sca}(\mathbf{r}) + \frac{\psi_l'(kr)}{kr}\left[\tau_{lm}(\theta)\hat{\theta} \times \mathbf{J}_{sca}(\mathbf{r}) - i\pi_{lm}(\theta)\hat{\phi} \times \mathbf{J}_{sca}(\mathbf{r})\right] d^3r \quad (3)$$

$$a_M(l,m) = \frac{(-i)^{l+1}k^2\eta O_{lm}}{E_0[\pi(2l+1)]^{1/2}} \int e^{-im\phi} j_l(kr)\left[i\pi_{lm}(\theta)\hat{\theta} \times \mathbf{J}_{sca}(\mathbf{r}) + \tau_{lm}(\theta)\hat{\phi} \times \mathbf{J}_{sca}(\mathbf{r})\right] d^3r \quad (4)$$

where $\mathbf{J}_{sca}(\mathbf{r}) = -i\omega[\epsilon(\mathbf{r}) - \epsilon_h]\mathbf{E}(\mathbf{r})$ is the scattering current density as a function of permittivity the of surrounding host medium (ϵ_h) and total scattered field ($\mathbf{E}(\mathbf{r})$).

The multipolar expansion analysis reveals that the strongest contribution to the scattering cross section comes from MD and EQ resonances and that their relative spectral position and intensity change by changing the lattice constant (Figure 2). In detail, Figure 2a shows that at $P = 330$ nm, the dip in transmittance corresponds to an enhancement of the total scattering cross section, which is due to an enhancement of all the multipolar resonances, with a dominant contribution of the EQ resonance that accounts for about 50% of the total scattering cross section, and a relevant contribution from the MD resonances, whose relative weight is about 25%. The ED and MQ resonances are enhanced as well, but their contribution to the scattering cross section is weaker, below 15%. By increasing the lattice constant to $P = 340$ nm (Figure 2b), we observe a redshift of the resonant modes together with a narrowing of the lineshapes. In addition, the relative intensity of EQ and MD changes, and the two contributions account for 48% and 28%, respectively. The trend is confirmed by increasing the lattice constant to $P = 350$ nm (Figure 2c). Here, the EQ contribution falls to 40% and the MD contribution rises to 30%, and increasing P by an additional 10 nm (Figure 2d) results in an almost equal contribution of EQ and MD to the total scattering cross section, and by further increasing the lattice constant (Figure 2e–f), the MD resonance contribution becomes dominant.

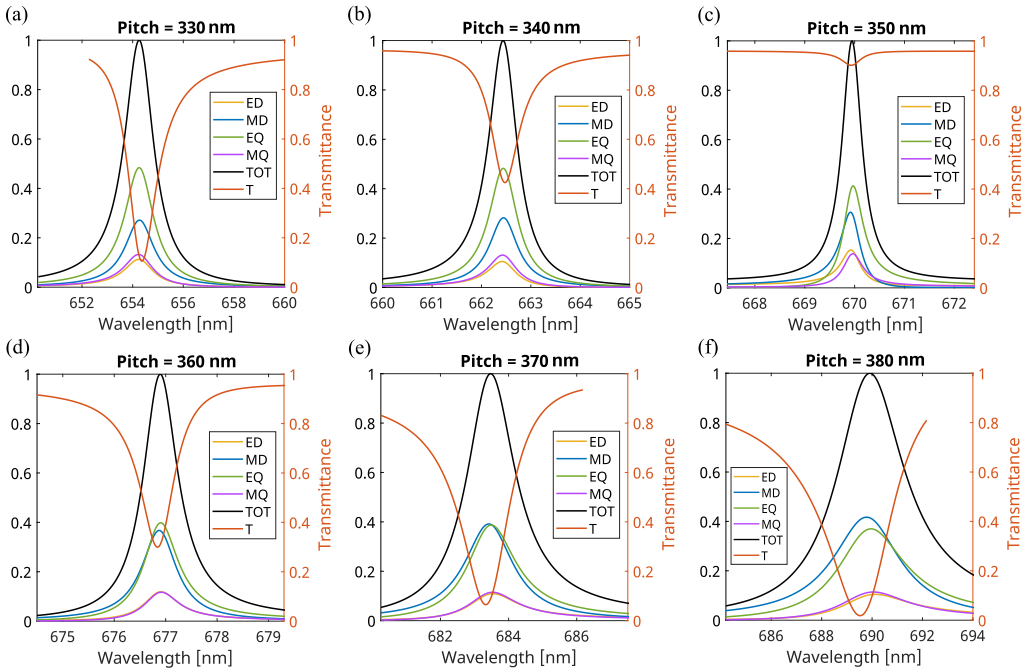

Figure 2. (**a**–**f**) Relative intensity of contributions from different multipolar resonances, including the electric dipole (ED), magnetic dipole (MD), electric quadrupole (EQ), and magnetic quadrupole (MQ), as well as the total sum of all contributions (TOT), assessed over a range of pitch values from 330 nm to 380 nm. On the left axis, the transmittance profile (T) is reported in red for the reader's convenience.

The role of the different multipolar resonances can be appreciated by looking at the field patterns within the nanopillars. The false-color maps on the top row in Figure 3 report the absolute value of the electric field distribution normalized with respect to the incident field for three representative values of P, namely, 330, 350 and 380 nm, while the normalized black arrows indicate the orientation of the electric field. The bottom row shows a sketch of the virtual multipoles excited within the pillar, where the transparency of the lines indicating the field direction has been adjusted to highlight the relative contribution of the individual multipolar resonance. The field is extracted along the xy plane at the center of the pillar at the resonant wavelength. At $P = 330$ nm, the field distribution shows two main lobes along the pillar corresponding to two out-of-phase dipoles constituting the EQ. Two weaker electric field loops in the upper and lower parts of the pillar can be identified by looking at the black arrows. At 350 nm, the field enhancement is greatly reduced, although the EQ is still visible. The attenuation corresponds to a weaker effect on the transmittance described above. At $P = 380$ nm, the two electric field loops originating the MD resonance are more clearly visible, while the field associated with the EQ resonance vanishes.

The effect of the lattice constant on the resonances can be addressed also by looking at the dependence of the Q-factor on P. It is well known that a collective response of the metasurface, with a spatially distributed mode over a large volume, can lead to a high Q resonance [53]. Figure 4a reports the Q factor calculated for the six values of the lattice constant P analyzed. Notably, we observe that the Q-factor peaks at a value of about 1400 for $P = 350$ nm, at which both the effect on the transmittance (Figure 2) and the field enhancement (Figure 3) are rather weak.

Besides the relative intensity variation of the multipolar resonances, by varying the lattice constant, a relative shift of the spectral position can be appreciated in Figure 2. To better estimate it, we reported in Figure 4b the difference between the relative scattering cross section of the EQ and MD resonances in the wavelength range near the resonance.

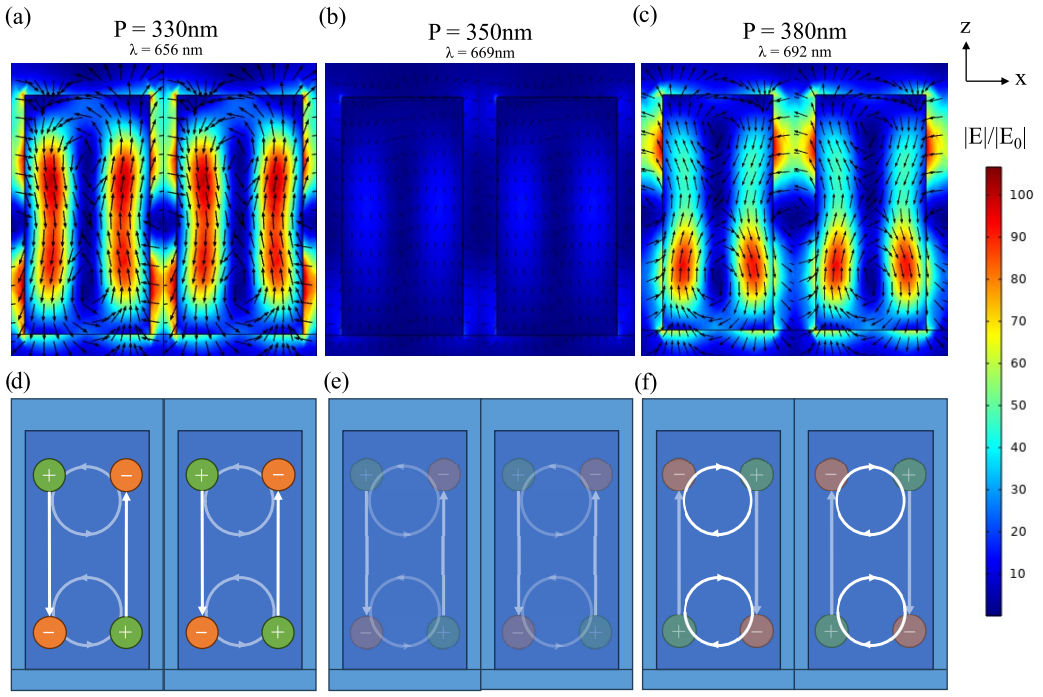

Figure 3. (**a**–**c**) Norm of the electric field intensity on the XZ plane, passing through the center of a pillar and one of its near neighbors. The black arrows indicate the orientation of the electric field component on the XZ plane. The electric field was evaluated for pillars with three different pitches P, (**a**) 330 nm, (**b**) 350 nm, and (**c**) 380 nm, and at their corresponding resonant wavelengths λ, (**a**) 656 nm, (**b**) 669 nm, and (**c**) 692 nm. (**d**–**f**) Schematic representation of the multipole displacement within the pillars. Dipoles with more intense coloring indicate a higher contribution for that specific combination of pitch and wavelength (λ).

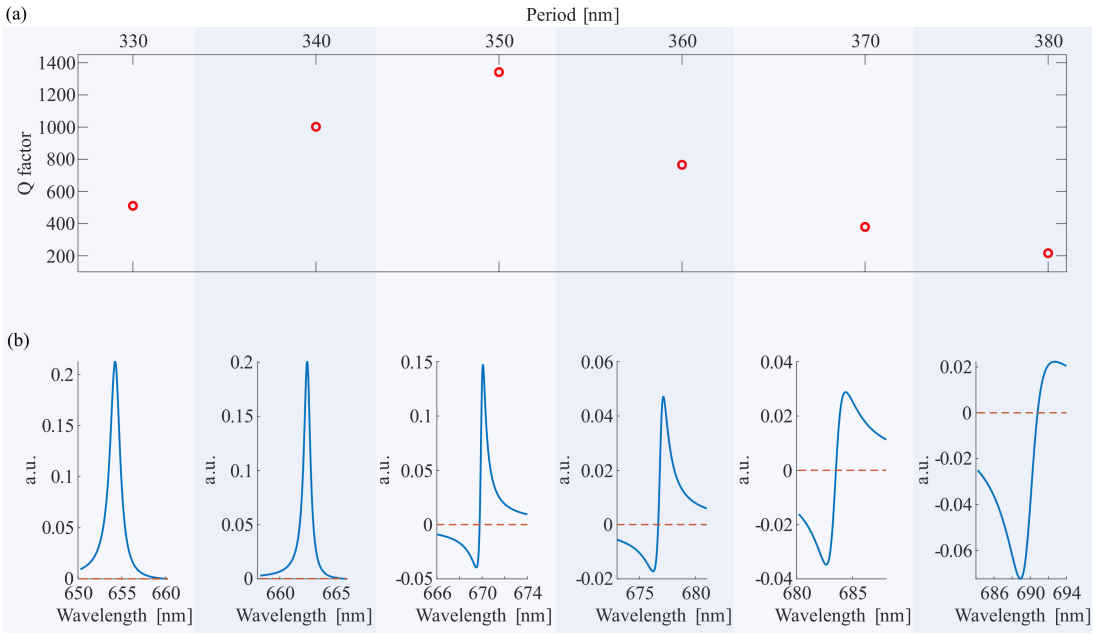

Figure 4. (**a**) Quality factors of the resonances for pillars with pitches ranging from 300 nm to 380 nm. (**b**) Difference in the scattering cross sections of the electric quadrupole (EQ) and magnetic dipole (MD) for the corresponding pitches (blue line). The red dashed line highlights the zero value.

At $P = 330$ nm, the lineshape is positive and symmetrical, indicating a spectral superposition of the two resonances with a prevalence of the EQ resonance. By increasing P to 340 nm, the lineshape becomes narrower (the Q-factor increases) and more asymmetric, which is even more visible at $P = 350$ nm, where the lineshape shows a negative peak at shorter wavelengths and a positive peak at larger wavelengths, meaning that the MD resonance undergoes a smaller redshift with respect to the EQ resonance. The different relative redshift is confirmed by further increasing the lattice constant P, and the spectral separation of the two modes becomes clearer, while the lineshape broadens.

The influence of the lattice parameter on the Fano resonances discussed in this paper can also be exploited in a sensing scheme, as the spectral position of the resonance is strongly affected by the distance between the pillars. In Figure 5, we report the resonant wavelength as a function of the lattice constant. The yellow vertical error bar in the graph indicates the FWHM for each point. By interpolating the data with a linear fit, we find a sensitivity, defined as $S = \frac{\Delta\lambda(\text{nm})}{\Delta P(\text{nm})} = 0.71$. The sensing performances of the proposed metasurface can be compared to similar systems by looking at the FOM, defined as the sensitivity divided by the FWHM of the resonance [54]:

$$FOM = \frac{S}{\Delta\lambda(\text{nm})} \tag{5}$$

Figure 5 on the right axis reports the FOM as a function of the pitch. The FOM peaks at 1.7 nm^{-1} when $P = 350$ nm, that is, where the Q-factor is maximum, and drops at a minimum value (in the wavelength range considered) of 0.2 nm^{-1}.

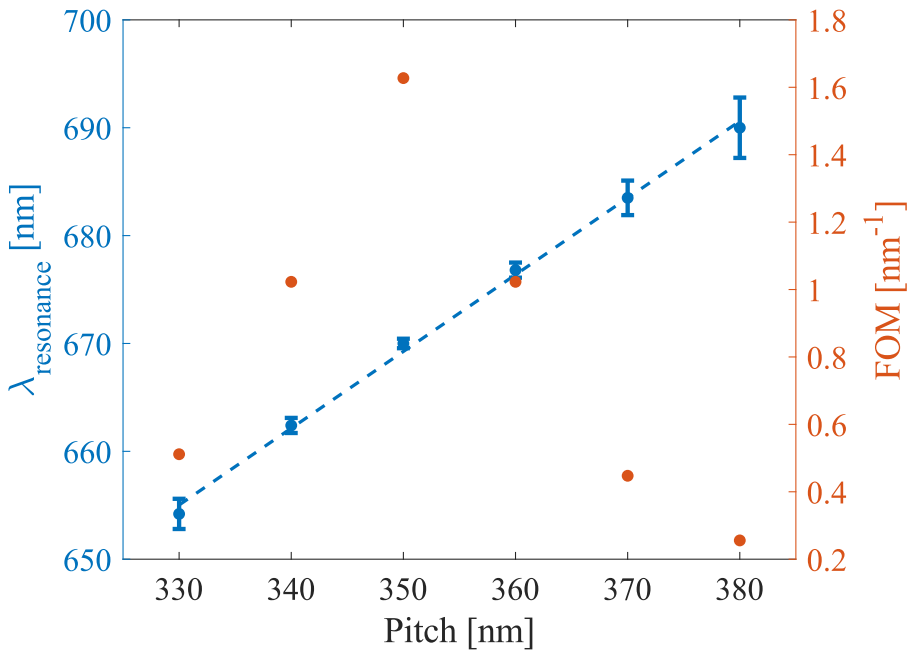

Figure 5. Resonance wavelength variation with the pitch of the metasurface (blue dashed line). The error bars indicate the full width at half maximum (FWHM) of the resonances (blue solid lines). Figure of Merit (red solid circles) evaluated for varying pitches.

4. Discussion and Conclusions

This paper reports a numerical analysis of the optical behavior of an all-dielectric metasurface based on a square lattice of cylindrical nanopillars. The resonant behavior results in a strong suppression of the forward scattering associated with the excitation of different multipolar resonances according to the Kerker conditions. We analyzed in detail the dependence of the resonant condition on the lattice constant, which affects the spectral

position, the lineshape, and the Q-factor of the resonances, revealing the collective response of the metasurface.

The reported result can be compared to a recent paper, where the case of ideal lossless nanopillars was considered [46], to highlight the role of the intrinsic losses. At the resonant condition, we indeed observe a strong enhancement of the absorption, especially for lower Q-factors, suggesting that light–matter interaction can be boosted within the nanopillars, which is crucial for many applications including nonlinear optics. Notably, intrinsic losses also have a dramatic effect when the Q-factor is maximized and the resonance lineshape approaches a symmetric condition: here, the resonance almost vanishes in the transmission spectrum, as does the field intensity within the nanopillars, while a reasonably high Q-factor is kept. Interestingly, such strong light intensity modulation can therefore be achieved either by modulating the pitch or by modulating the intrinsic losses.

By expanding the scattered field in a linear combination of the field scattered by electric and magnetic multipoles, we highlighted the preeminent role of MD and EQ resonances and how their relative spectral position and intensity affect the lineshape and Q-factor of the resonance. Interestingly, we found that forward-scattering suppression is greatly attenuated when the Q-factor is maximized, and the metasurface becomes almost perfectly transparent. Such an effect can also be interpreted in terms of the field distribution, where at $P = 350$ nm the local field is strongly attenuated as if destructive interference occurs within the nanopillar. The lattice parameter indeed has an impact on the field distributions, which change from a single loop at lower values of the lattice constant to a double loop at higher values. The strong tunability of the transmittance shown by the structure can be exploited for light-intensity optomechanical modulators by applying mechanical strain if the structure is fabricated on an elastic support [55,56]. The structural parameter changes and the related spectral shift induced can also be exploited in an optical sensing scheme, where white-light illumination can be employed to monitor the resonance shift. The sensitivity found for the proposed metasurface is 0.71 nm of resonant wavelength shift per nm of pitch variation, while the FOM is between a minimum of 0.2 and a maximum of 1.7 nm^{-1}. Such values and the Q-factor can be compared to other similar structures reported in [57].

We underline that the structure under investigation shows a strong resonant behavior with a Q-factor as high as 1400 despite the simplicity of the geometry of the individual nanoscatterer, which enables the use of self-assembling fabrication techniques for a scalable and cost-effective fabrication of a metasurface based photonic devices [58].

Author Contributions: Conceptualization, A.A.; methodology, V.B.; software, V.B.; investigation, V.B.; resources, A.A.; data curation, A.A. and V.B.; writing—original draft preparation, V.B.; writing—review and editing, A.A.; supervision, A.A.; funding acquisition, A.A. All authors have read and agreed to the published version of the manuscript.

Funding: This research and the APC were funded by the Ministero dell'Università e della Ricerca (Project PRIN PETALS Grant No. 2020TS9LXS).

Data Availability Statement: The authors agree to make data and materials supporting the results or analyses presented in their paper available upon reasonable request.

Conflicts of Interest: The authors declare no conflicts of interest.

Abbreviations

The following abbreviations are used in this manuscript:

ED	electric dipole
MD	magnetic dipole
EQ	electric quadrupole
MQ	Magnetic Quadrupole

References

1. Jahani, S.; Jacob, Z. All-dielectric metamaterials. *Nat. Nanotechnol.* **2016**, *11*, 23–36. [CrossRef] [PubMed]
2. Khorasaninejad, M.; Capasso, F. Metalenses: Versatile multifunctional photonic components. *Science* **2017**, *358*, eaam8100. [CrossRef]
3. Nookala, N.; Lee, J.; Tymchenko, M.; Gomez-Diaz, J.S.; Demmerle, F.; Boehm, G.; Lai, K.; Shvets, G.; Amann, M.C.; Alu, A.; et al. Ultrathin gradient nonlinear metasurface with a giant nonlinear response. *Optica* **2016**, *3*, 283. [CrossRef]
4. Liu, Z.; Xu, Y.; Lin, Y.; Xiang, J.; Feng, T.; Cao, Q.; Li, J.; Lan, S.; Liu, J. High-Q Quasibound States in the Continuum for Nonlinear Metasurfaces. *Phys. Rev. Lett.* **2019**, *123*, 253901. [CrossRef]
5. Hähnel, D.; Golla, C.; Albert, M.; Zentgraf, T.; Myroshnychenko, V.; Förstner, J.; Meier, C. A multi-mode super-fano mechanism for enhanced third harmonic generation in silicon metasurfaces. *Light Sci. Appl.* **2023**, *12*, 97. [CrossRef]
6. Prokhorov, A.V.; Gubin, M.Y.; Shesterikov, A.V.; Arsenin, A.V.; Volkov, V.S.; Evlyukhin, A.B. Lasing Effect in Symmetrical van der Waals Heterostructured Metasurfaces Due to Lattice-Induced Multipole Coupling. *Nano Lett.* **2023**, 23, 11105–11111. [CrossRef]
7. Hemmatyar, O.; Abdollahramezani, S.; Kiarashinejad, Y.; Zandehshahvar, M.; Adibi, A. Full color generation with Fano-type resonant HfO_2 nanopillars designed by a deep-learning approach. *Nanoscale* **2019**, *11*, 21266. [CrossRef]
8. Altug, H.; Oh, S.H.; Maier, S.A.; Homola, J. Advances and applications of nanophotonic biosensors. *Nat. Nanotechnol.* **2022**, *17*, 5–16. [CrossRef] [PubMed]
9. Chen, H.; Fan, X.; Fang, W.; Zhang, B.; Cao, S.; Sun, Q.; Wang, D.; Niu, H.; Li, C.; Wei, X.; et al. High-Q Fano resonances in all-dielectric metastructures for enhanced optical biosensing applications. *Biomed. Opt. Express* **2024**, *15*, 294–305. [CrossRef]
10. Zhao, H.; Fan, X.; Wei, X.; Li, C.; Zhao, T.; Fang, W.; Niu, H.; Bai, C.; Kumar, S. Highly sensitive multiple fano resonances excitation on all-dielectric metastructure. *Opt. Rev.* **2023**, *30*, 208–216. [CrossRef]
11. Benea-Chelmus, I.C.; Mason, S.; Meretska, M.L.; Elder, D.L.; Kazakov, D.; Shams-Ansari, A.; Dalton, L.R.; Capasso, F. Gigahertz free-space electro-optic modulators based on Mie resonances. *Nat. Commun.* **2022**, *13*, 3170. [CrossRef] [PubMed]
12. Li, W.; Liu, M.; Cheng, S.; Zhang, H.; Yang, W.; Yi, Z.; Zeng, Q.; Tang, B.; Ahmad, S.; Sun, T. Polarization independent tunable bandwidth absorber based on single-layer graphene. *Diam. Relat. Mater.* **2024**, *142*, 110793. [CrossRef]
13. Wang, K.; Titchener, J.G.; Kruk, S.S.; Xu, L.; Chung, H.P.; Parry, M.; Kravchenko, I.I.; Chen, Y.H.; Solntsev, A.S.; Kivshar, Y.S.; et al. Quantum Metasurface for Multiphoton Interference and State Reconstruction. *Science* **2018**, *361*, 1104–1108. [CrossRef]
14. Redit, C.; Ommo, C. Metasurfaces go mainstream. *Nat. Photonics* **2023**, *17*, 6. [CrossRef]
15. Shah, Y.D.; Dada, A.C.; Grant, J.P.; Cumming, D.R.S.; Altuzarra, C.; Nowack, T.S.; Lyons, A.; Clerici, M.; Faccio, D. An All-Dielectric Metasurface Polarimeter. *ACS Photonics* **2022**, *9*, 3245–3252. [CrossRef] [PubMed]
16. Zheng, Z.; Zhu, Y.; Duan, J.; Qin, M.; Wu, F.; Xiao, S. Enhancing Goos-Hänchen shift based on magnetic dipole quasi-bound states in the continuum in all-dielectric metasurfaces. *Opt. Express* **2021**, *29*, 29541–29549. [CrossRef] [PubMed]
17. Capasso, F. Metaoptics for the consumer market. *Nat. Photonics* **2023**, *17*, 6–7. [CrossRef]
18. Pourmand, M.; Choudhury, P.K., Light-Matter Interaction at the Sub-Wavelength Scale: Pathways to Design Nanophotonic Devices. In *Adventures in Contemporary Electromagnetic Theory*; Mackay, T.G., Lakhtakia, A., Eds.; Springer International Publishing: Cham, Switzerland, 2023; pp. 281–314. [CrossRef]
19. Cheben, P.; Halir, R.; Schmid, J.H.; Atwater, H.A.; Smith, D.R. Subwavelength integrated photonics. *Nature* **2018**, *560*, 565–570. [CrossRef]
20. Yue, Z.; Li, J.; Li, J.; Zheng, C.; Liu, J.; Wang, G.; Xu, H.; Chen, M.; Zhang, Y.; Zhang, Y.; et al. Terahertz metasurface zone plates with arbitrary polarizations to a fixed polarization conversion. *Opto-Electron. Sci.* **2022**, *1*, 210014-1–210014-8. [CrossRef]
21. Kowerdziej, R.; Wróbel, J.; Kula, P. Ultrafast electrical switching of nanostructured metadevice with dual-frequency liquid crystal. *Sci. Rep.* **2019**, *9*, 20367. [CrossRef]
22. Wang, Y.; Jia, S.; Qin, J. Tunable Fano Resonance and Enhanced Sensing in Terahertz Metamaterial. *Front. Phys.* **2021**, *8*, 605125. [CrossRef]
23. Sajedian, I.; Lee, H.; Rho, J. Double-deep Q-learning to increase the efficiency of metasurface holograms. *Sci. Rep.* **2019**, *9*, 10899. [CrossRef] [PubMed]
24. Ma, Q.; Liu, C.; Xiao, Q.; Gua, Z.; Gao, X.; Li, L.; Cui, T.J. Information metasurfaces and intelligent metasurfaces. *Photonics Insights* **2022**, *1*, R01. [CrossRef]
25. Malkiel, I.; Mrejen, M.; Nagler, A.; Arieli, U.; Wolf, L.; Suchowski, H. Plasmonic nanostructure design and characterization via Deep Learning. *Light Sci. Appl.* **2018**, *7*, 60. [CrossRef] [PubMed]
26. Seong, J.; Jeon, Y.; Yang, Y.; Badloe, T.; Rho, J. Cost-Effective and Environmentally Friendly Mass Manufacturing of Optical Metasurfaces Towards Practical Applications and Commercialization. *Int. J. Precis. Eng. Manuf.-Green Technol.* **2023**, *11*, 685–706. [CrossRef]
27. Estakhri, N.M.; Edwards, B.; Engheta, N. Inverse-designed metastructures that solve equations. *Science* **2019**, *363*, 1333–1338. [CrossRef] [PubMed]
28. Pile, D. Metamaterials for the masses. *Nat. Photonics* **2023**, *17*, 2–3. [CrossRef]
29. Hu, Y.; Wang, X.; Luo, X.; Ou, X.; Li, L.; Chen, Y.; Yang, P.; Wang, S.; Duan, H. All-dielectric metasurfaces for polarization manipulation: Principles and emerging applications. *Nanophotonics* **2020**, *9*, 3755–3780. [CrossRef]
30. Liu, S.; Vabishchevich, P.P.; Vaskin, A.; Reno, J.L.; Keeler, G.A.; Sinclair, M.B.; Staude, I.; Brener, I. An all-dielectric metasurface as a broadband optical frequency mixer. *Nat. Commun.* **2018**, *9*, 2507. [CrossRef]

31. Lincoln, R.L.; Scarpa, F.; Ting, V.P.; Trask, R.S. Multifunctional composites: A metamaterial perspective. *Multifunct. Mater.* **2019**, *2*, 043001. [CrossRef]
32. Zeng, C.; Lu, H.; Mao, D.; Du, Y.; Hua, H.; Zhao, W.; Zhao, J. Graphene-empowered dynamic metasurfaces and metadevices. *Opto-Electron. Adv.* **2022**, *5*, 200098. [CrossRef]
33. Kerker, M.; Wang, D.S.; Giles, C.L. Electromagnetic scattering by magnetic spheres. *J. Opt. Soc. Am.* **1983**, *73*, 765–767. [CrossRef]
34. Barreda, A.; Albella, P.; Moreno, F.; González, F. Broadband Unidirectional Forward Scattering with High Refractive Index Nanostructures: Application in Solar Cells. *Molecules* **2021**, *26*, 4421. [CrossRef]
35. Valero, A.C.; Shamkhi, H.K.; Kupriianov, A.S.; Weiss, T.; Pavlov, A.A.; Redka, D.; Bobrovs, V.; Kivshar, Y.; Shalin, A.S. Superscattering emerging from the physics of bound states in the continuum. *Nat. Commun.* **2023**, *14*, 4689. [CrossRef]
36. Alaee, R.; Filter, R.; Lehr, D.; Lederer, F.; Rockstuhl, C. A generalized Kerker condition for highly directive nanoantennas. *Opt. Lett.* **2015**, *40*, 2645. [CrossRef]
37. Zhang, Z.; Liu, P.; Lu, W.; Bai, P.; Zhang, B.; Chen, Z.; Maier, S.A.; Gómez Rivas, J.; Wang, S.; Li, X. High-Q collective Mie resonances in monocrystalline silicon nanoantenna arrays for the visible light. *Fundam. Res.* **2023**, *3*, 822–830. [CrossRef]
38. Cara, E.; Lupi, F.F.; Fretto, M.; Leo, N.D.; Tortello, M.; Gonnelli, R.; Sparnacci, K.; Boarino, L. Directed Self-Assembly of Polystyrene Nanospheres by Direct Laser-Writing Lithography. *Nanomaterials* **2020**, *10*, 280. [CrossRef] [PubMed]
39. Jonsson, M.P.; Dahlin, A.B.; Jönsson, P.; Höök, F. Nanoplasmonic biosensing with focus on short-range ordered nanoholes in thin metal films. *Biointerphases* **2008**, *3*, FD30–FD40. [CrossRef] [PubMed]
40. Murataj, I.; Channab, M.; Cara, E.; Pirri, C.F.; Boarino, L.; Angelini, A.; Lupi, F.F. Hyperbolic Metamaterials via Hierarchical Block Copolymer Nanostructures. *Adv. Opt. Mater.* **2021**, *9*, 2001933. [CrossRef]
41. Huang, C.; Zhu, Y.; Man, X. Block copolymer thin films. *Phys. Rep.* **2021**, *932*, 1–36. [CrossRef]
42. Yang, G.G.; Choi, H.J.; Han, K.H.; Kim, J.H.; Lee, C.W.; Jung, E.I.; Jin, H.M.; Kim, S.O. Block Copolymer Nanopatterning for Nonsemiconductor Device Applications. *ACS Appl. Mater. Interfaces* **2022**, *14*, 12011–12037. [CrossRef]
43. Greybush, N.J.; Pacheco-Peña, V.; Engheta, N.; Murray, C.B.; Kagan, C.R. Plasmonic Optical and Chiroptical Response of Self-Assembled Au Nanorod Equilateral Trimers. *ACS Nano* **2019**, *13*, 1617–1624. [CrossRef] [PubMed]
44. Phillip, H.R.; Taft, E.A. Kramers-Kronig Analysis of Reflectance Data for Diamond. *Phys. Rev.* **1964**, *136*, A1445–A1448. [CrossRef]
45. SCHOTT North America, I. Optical Glass Data Sheets. Available online: https://www.schott.com/en-ie/products/optical-glass-P1000267/downloads (accessed on 8 February 2024).
46. Bonino, V.; Angelini, A. High-Q Fano Resonances in Diamond Nanopillars. *Opt. Mater. Express* **2023**, *13*, 1110. [CrossRef]
47. Lin, R.; Alnakhli, Z.; Alqatari, F.; Li, X. Analysis of Tapered Nanopillars for Reflective Metalens: The Role of Higher-Order Modes. *IEEE Photonics J.* **2020**, *12*, 4600907. [CrossRef]
48. Miroshnichenko, A.E.; Flach, S.; Kivshar, Y.S. Fano resonances in nanoscale structures. *Rev. Mod. Phys.* **2010**, *82*, 2257–2298. [CrossRef]
49. Limonov, M.F.; Rybin, M.V.; Poddubny, A.N.; Kivshar, Y.S. Fano Resonances in Photonics. *Nat. Photonics* **2017**, *11*, 543–554. [CrossRef]
50. Riccardi, M.; Kiselev, A.; Achouri, K.; Martin, O.J.F. Multipolar expansions for scattering and optical force calculations beyond the long wavelength approximation. *Phys. Rev. B* **2022**, *106*, 115428. [CrossRef]
51. Grahn, P.; Shevchenko, A.; Kaivola, M. Electromagnetic Multipole Theory for Optical Nanomaterials. *New J. Phys.* **2012**, *14*, 093033. [CrossRef]
52. Mühlig, S.; Menzel, C.; Rockstuhl, C.; Lederer, F. Multipole Analysis of Meta-atoms. *Metamaterials* **2011**, *5*, 64–73. [CrossRef]
53. Yang, Y.; Kravchenko, I.I.; Briggs, D.P.; Valentine, J. All-dielectric metasurface analogue of electromagnetically induced transparency. *Nat. Commun.* **2014**, *5*, 5753. [CrossRef] [PubMed]
54. Su, W.; Ding, Y.; Luo, Y.; Liu, Y. A high figure of merit refractive index sensor based on Fano resonance in all-dielectric metasurface. *Results Phys.* **2020**, *16*, 102833. [CrossRef]
55. Zhang, C.; Jing, J.; Wu, Y.; Fan, Y.; Yang, W.; Wang, S.; Song, Q.; Xiao, S. Stretchable All-Dielectric Metasurfaces with Polarization-Insensitive and Full-Spectrum Response. *ACS Nano* **2020**, *14*, 1418–1426. [CrossRef] [PubMed]
56. Gutruf, P.; Zou, C.; Withayachumnankul, W.; Bhaskaran, M.; Sriram, S.; Fumeaux, C. Mechanically Tunable Dielectric Resonator Metasurfaces at Visible Frequencies.*ACS Nano* **2016**, *10*, 133–141. [CrossRef]
57. Chen, X.; Zhang, Y.; Cai, G.; Zhuo, J.; Lai, K.; Ye, L. All-dielectric metasurfaces with high Q-factor Fano resonances enabling multi-scenario sensing. *Nanophotonics* **2022**, *11*, 4537–4549. [CrossRef]
58. Bonakdar, A.; Jang, S.J.; Brown, R.L.; Rezaei, M.; Mohseni, H. Deep UV microsphere nanolithography to achieve sub-100 nm feature size. In *Nanoengineering: Fabrication, Properties, Optics, and Devices XI*; SPIE: San Diego, CA, USA, 2014; Volume 9170, pp. 143–148. [CrossRef]